ELSEVIER

Physica A 210 (1994) 87–112

PHYSICA A

Multiple light scattering in Taylor-Couette flow

D. Bicout [1,2], G. Maret [3]

High Magnetic Field Laboratory,
Max-Planck Institut für Festkörperforschung and Centre National de la Recherche Scientifique,
25 avenue des Martyrs, B.P. 166, F-38042 Grenoble Cedex 9, France

Received 9 November 1993; revised 28 April 1994

Abstract

We report dynamic light scattering experiments on turbid colloidal suspension under stationary and laminar flow, as well as in the regime of flow instabilities. It is shown that the time autocorrelation function $C_1(t) = \langle E(0)E^*(t)\rangle/\langle|E(0)|^2\rangle$ of the scattered light field $E(t)$ is not sensitive to the mean velocity flow but rather to the root mean square of velocity gradient. $C_1(t)$ is characterised on the level of each scattering event by the correlation time required by a pair of scatterers initially separated by a transport mean free path to move a relative distance of optical wavelength due to the velocity gradient. We verified this theoretical analysis using planar Couette flow as an example for homogeneous velocity gradients, and planar Poiseuille flow for inhomogeneous velocity gradients. Agreement between experiment and theory is excellent. Finally, this technique is applied to spatially varying velocity gradient fields for measuring the threshold and wave number of the Taylor-Couette instability. This illustrates the possibility of studying hydrodynamic instabilities and quasi-local velocity gradients even under conditions of strong multiple scattering.

[1] And Université Joseph Fourier, UFR de Physique, B.P. 53X, F-38041 Grenoble Cedex, France.
[2] Present address: Institut de Biologie Structurale, 41 avenue des Martyrs, F-38027 Grenoble Cedex 01, France.
[3] Present address: Institut Charles Sadron, CNRS, 6, rue Boussingault, F-67083 Strasbourg Cedex, France.

SSDI 0378-4371(94)00101-X

1. Introduction

One of the most important techniques to measure velocities in flowing fluids is Quasi Elastic Light Scattering (QELS) [1,2], since this method is both accurate and non-invasive. Application of this technique requires a small concentration of the scattering particles which serve as markers by flowing with the fluid, so that only single scattering occurs. Many colloidal suspensions of technological and fundamental interest, however, are turbid i.e. show multiple scattering of light because of elevated concentrations of strongly scattering particles. It is therefore important to develop techniques that cope with this. Wu et al. [3] have shown that the temporal fluctuations of the multiply scattered light intensity can be analysed, along the lines developed to study Brownian motion [4–6] in dense colloidal suspensions, to measure a mean square velocity gradient in laminar planar Poiseuille flow. This rather novel technique is sometimes called Diffusing Wave Spectroscopy (DWS) [5].

In this paper, we show that by comparing measurements in different scattering geometries (homogeneous, inhomogeneous and spatially periodic velocity gradient fields) with the appropriate theory, quantitative information about quasi local velocity gradients and hydrodynamic instabilities can be obtained. In the first part of this paper, we resume the theoretical developments [7,8], which are necessary to determine the root mean square of the velocity gradient from the measured temporal autocorrelation function of light multiply scattered from small particles immersed in a steady laminar flow. In the second part, we report experimental results on steady and laminar planar Couette and Poiseuille flows which critically test the method for homogeneous and inhomogeneous velocity gradient fields, respectively. All relevant physical quantities are measured independently, allowing for a quantitative comparison of theory and experiment without adjustable parameters. Finally, in the third part, we extend the method beyond the hydrodynamic Taylor-Couette instability. Both the experimental results and theoretical analysis allow to measure the threshold and wave number of hydrodynamic instabilities, and to monitor quasi local velocity gradients up to Reynolds numbers well above threshold.

2. Theory

In quasielastic multiple light scattering experiments, the motion of particles is probed by monitoring the time autocorrelation function $C_1(t) = \langle E(0)E^*(t)\rangle/\langle|E(0)|^2\rangle$, where $E(t)$ is the scattered electric field of light collected by the detector. Experimentally, the intensity autocorrelation function $\langle I(t)I(0)\rangle/\langle I(0)\rangle^2$ is determined rather than $C_1(t)$. When the scattered electric fields are Gaussian distributed, $C_1(t)$ is related to the intensity autocorrelation function by the Siegert relation [9]:

$$\frac{\langle I(t)I(0)\rangle}{\langle I(0)\rangle^2} = 1 + |C_1(t)|^2$$

To compute $C_1(t)$ we consider light which is multiply scattered by a random distribution of point-like particles, and hence executes a random walk through the sample. Within the weak scattering limit ($kl \gg 1$; k and l being the wave number and the scattering mean free path of light, respectively) and in the strong multiple scattering regime ($L \gg l$; L being the linear dimension of the sample cell), the intensity of light leaving the sample can be described in the diffusion approximation [10]. The time autocorrelation function is given by [3,4,6,10,11]:

$$C_1(t) = I_0 \sum_{n=1}^{\infty} P(n)\langle \exp\{i\Delta\phi_n(t)\}\rangle \tag{1}$$

where $P(n)$, the fraction of total intensity I_0 scattered in all n^{th} order scattering paths, describes the diffusive transport of light and is related to the sample geometry. $\Delta\phi_n(t) = \sum_{\nu=1}^{n} \mathbf{q}_\nu \cdot \Delta\mathbf{r}_\nu(t)$ is thus the phase difference of the scattered electric field between time $t = 0$ and t, associated to a given multiple scattering paths of n^{th} order, and contains the dynamical information about the scatterers. $\langle \cdots \rangle$ denotes both the configurational average of $\Delta\mathbf{r}_\nu(t) = \mathbf{r}_\nu(t) - \mathbf{r}_\nu(0)$ (displacements during time t of ν^{th} scatterer) and the average over all possible scattering wave vectors $\mathbf{q}_\nu = \mathbf{k}_\nu - \mathbf{k}_{\nu-1}$. We consider now a fluid under laminar stationary flow, containing independent elastic scatterers which follow the fluid motion. In addition to the motion imposed by the fluid, the scatterers undergo also a Brownian motion because of finite temperature. If Brownian motion is not affected by the velocity gradient field, i.e. when the Taylor dispersion [12,13] can be neglected, the total displacement of a scatterer can be separated into a diffusive and convective part. Then we can treat separately the decorrelation of scattered fields due to these two independent motions. For Brownian motion, the derivation of the averaged quantity of Eq. (1) can be found in Refs 4 and 6. In order to describe the decorrelation caused by the flow, we make the following assumptions:

(i) The properties of multiple scattering of light are not affected by the flow, there is no correlation between the scattering mean free path and the velocity field and its derivative.

(ii) The velocity field varies slowly at the scale of scattering mean free path. This implies that the scattering mean free path is much smaller than the dissipation scale of flow.

(iii) The flow is stationary or quasi-stationary. This means that the characteristic time scale of the time autocorrelation function is smaller than the characteristic time scale of velocity changes.

One can show [7] that, for incompressible fluids, the leading non vanishing term in a cumulant expansion of Eq. (1) is the second cumulant which

corresponds to the fluctuations of the phase difference. We have: $\langle \cdots \rangle = \exp\{-\langle \Delta\phi_n^2(t) \rangle/2\}$, where the fluctuations of $\Delta\phi_n(t)$ are given by the relation [7,8]:

$$\langle \Delta\phi_n^2(t) \rangle = \tfrac{2}{15} (klt)^2 n \varepsilon(n) \tag{2}$$

and $\varepsilon(n)$ is defined as:

$$\varepsilon(n) = 2 \sum_{i,j} \left\{ \int \sigma_{ij}^2(\mathbf{r})\ \rho_n(\mathbf{r})\, d^3\mathbf{r} \right\}; \qquad i,j = x,y,z \tag{3}$$

where $\sigma_{ij} = \frac{1}{2}(\partial_i V_j + \partial_j V_i)$ is the strain tensor, and $\rho_n(\mathbf{r})$ is the end-to- end local density distribution of diffusion path of n^{th} order [7,8]. This distribution depends upon the geometry of the sample. $\varepsilon(n)$ is the expectation value of the square of the strain tensor weighted by the cloud of light paths. $\varepsilon(n)$ describes the fact that due to the spatial variation of the strain tensor, the dephasing of light is not the same everywhere in the scattering medium: For each geometrically different n^{th} order scattering path, one expects a different contribution to the dephasing of light. Thus systems with homogeneous velocity gradients over the whole scattering medium are distinct from systems with inhomogeneous velocity gradients.

2.1. Homogeneous system: Planar Couette flow

Planar Couette flow is the simplest homogeneous system. The velocity profile is $\mathbf{V} = \Gamma x \boldsymbol{e}_z$ where Γ is the shear rate and $\boldsymbol{e}_z$ the flow direction. The non zero element of the strain tensor is: $\sigma_{xz} = \Gamma/2$. Therefore, $\varepsilon(n) = \Gamma^2$, and the fluctuations of the phase difference can be written as:

$$\langle \Delta\phi_n^2(t) \rangle = 4(t/\tau_c)^2 n \tag{4}$$

where $\tau_c = \sqrt{30}/kl\Gamma$ is the characteristic time needed by a pair of scatterers initially separated by a distance l to move a relative distance λ due to the velocity gradient Γ. Taking into account Brownian motion, we thus have:

$$\langle \exp\{i\Delta\phi_n(t)\} \rangle = \exp\{-(t/2\tau_0)\, n - 2(t/\tau_c)^2 n\} \tag{5}$$

with $\tau_0 = 1/4k^2 D_B$, where D_B is the diffusion constant of the scatterer. The time autocorrelation function is therefore given by:

$$C_1(t) = \int_1^\infty P(n) \exp\{-(t/2\tau_0)\, n - 2(t/\tau_c)^2 n\}\, dn \tag{6}$$

where we have taken the continuum limit by replacing in Eq. (1) the sum over n by integral. $C_1(t)$ has two independent time scales, τ_0 and τ_c, corresponding to the Brownian motion and shear of planar Couette flow, respectively. In zero

shear ($\Gamma = 0$), $C_1(t)$ has an exponential decay $\exp\{-(t/2\tau_0)\}$ per scattering event, which is characteristic of stochastic motion. When Brownian motion is neglected, $C_1(t)$ has a Gaussian decay $\exp\{-2(t/\tau_c)^2\}$ per scattering event, which is characteristic of deterministic motion. In general, the decay of $C_1(t)$ is dominated by Brownian motion at short times $t < (\tau_c^2/4\tau_0)$ and by shear flow at long times $t > (\tau_c^2/4\tau_0)$. The final expression of $C_1(t)$ is obtained by integration over $P(n)$ for a given experimental geometry. For reflection of an extended plane wave source from a slab of thickness L, we obtain [11]:

$$C_1(t) = \frac{1}{1-\gamma l/L} \frac{\sinh\left[(L/l-\gamma)\sqrt{6(t/\tau_c)^2 + (3t/2\tau_0)}\right]}{\sinh\left[(L/l)\sqrt{6(t/\tau_c)^2 + (3t/2\tau_0)}\right]} \tag{7}$$

γ (see Section 3) is a coefficient related to the boundary conditions of transport of light through the sample. In the limit $L/l \gg 1$ (thick medium), we have: $C_1(t) = \exp\{-\gamma\sqrt{6(t/\tau_c)^2 + (3t/2\tau_0)}\}$.

2.2. *Inhomogeneous system: Planar Poiseuille flow*

The velocity profile of planar Poiseuille flow is $\mathbf{V} = \frac{\Gamma}{L}(Lx - x^2)\mathbf{e}_z$; $0 \leq x \leq L$, and the strain tensor is a linear function of x: $\sigma_{xz} = \frac{\Gamma}{2}(1 - 2x/L)$. In this case, the computation of $\langle \Delta\phi_n^2(t)\rangle$ requires the evaluation of the integral of Eq. (3). The key for this is the determination of $\rho_n(\mathbf{r})$ for a given experimental geometry. We consider here the multiply scattered light transmitted through a slab of thickness L. This results in an effective velocity gradient Γ_{eff} [7]:

$$\frac{\Gamma_{eff}^2}{\Gamma^2} = \frac{1}{3} - \frac{2}{\pi^2} + \frac{16}{\pi^2}\sum_{m=3}^{\infty}[1-(-1)^m]\frac{m}{(m^2-1)^2}\frac{\sin[m\pi l/L]}{\sin[\pi l/L]} \times \exp\left[-\frac{(m^2-1)\pi^2 l}{6L}\right] \tag{8}$$

and, the fluctuations of the phase difference in transmission take the form:

$$\langle \Delta\phi_n^2(t)\rangle = 4(t/\tau_p)^2 n \tag{9}$$

where $\tau_p = \sqrt{30}/kl\Gamma_{eff}$. τ_p has the same definition as τ_c given above, and can be considered as the characteristic correlation time corresponding to the presence of an effective shear rate Γ_{eff} caused by the planar Poiseuille flow. $C_1(t)$ is given as in Eq. (6), except that τ_c is replaced by τ_p. In the case of transmission through a slab illuminated by a plane wave source, the time autocorrelation function is given by [11]:

$$C_1(t) = \frac{L}{\gamma l} \frac{\sinh\left[\gamma\sqrt{6(t/\tau_p)^2 + (3t/2\tau_0)}\right]}{\sinh\left[(L/l)\sqrt{6(t/\tau_p)^2 + (3t/2\tau_0)}\right]} \tag{10}$$

Thus for transmission, the characteristic decay time of $C_1(t)$ is $(l/L)^2\tau_0$ if $\tau_0 \ll \tau_p$ and is $(l/L)\tau_p$ if $\tau_0 \gg \tau_p$ (except for small time window at $t < (l/L)(\tau_p^2/4\tau_0)$). $C_1(t)$ takes a simple form when the shear dominates the decay. In the limit $\tau_p \ll (l/L)\tau_0$, we have:

$$C_1(t) \simeq \begin{cases} 1 - (t/\tau_T)^2; & (l/L)(\tau_p^2/4\tau_0) < t < \tau_T \\ 2\sqrt{6}\dfrac{t}{\tau_T}\exp\{-\sqrt{6}\dfrac{t}{\tau_T}\}; & \tau_T < t < \tau_p \end{cases} \tag{11}$$

with $\tau_T = l\tau_p/L = \sqrt{(30)}/kL\Gamma_{eff}$. Note that, despite of the strong multiple scattering, $C_1(t)$ in transmission does not depend on the quantities l and γ describing the multiple scattering properties of the medium. Therefore Γ_{eff} can be obtained without particular knowledge of these properties.

We have considered so far suspensions of noninteracting small particles of size (a) much smaller than the optical wavelength λ (Rayleigh regime or isotropic scattering). However, in many experimental situations, particles are larger size ($a \geq \lambda$, Mie regime) and light is scattered anisotropically [14]. This leads to a transport mean free path l^* in the description of light transport which is larger than the scattering mean free path l. l^* and l are related through the particle form factor $F(\mathbf{q})$ [15]:

$$\frac{l^*}{l} = \frac{2k^2 \int F(q)\, q\, dq}{\int q^2 F(q)\, q\, dq}$$

Maret and Wolf have shown [4] that for particles undergoing Brownian motion, $C_1(t)$ obtained for point like scatterers and for Mie scatterers are exactly the same provided that l is everywhere replaced by l^*. This fact remains still valid for the case of flows as long as the velocity field varies slowly at the scale l^* (see Appendix A).

3. Experimental

3.1. Set-up

We used a vertically polarized beam of mono-mode Ar^+ laser ($\lambda = 514.5$ nm) beam incident on the sample cell. Less than one coherence area [9] of the vertical component of the scattered light is collected onto a photomultiplier tube (VV-configuration). From the photomultiplier output $I(t)$ the normalized intensity autocorrelation function $C_2(t)$ is determined using a PC- controlled digital multibit correlator with up to 1024 channels. From the PC we obtain the time field autocorrelation function $C_1(t)$. Because the area of observation of scattered light cannot be infinitesimally small compared to the coherence area [9], $C_2(0)$ and $C_1(0)$ are experimentally always somewhat smaller than 2

and 1, respectively. Quantitative comparison between experiments and theory is made by normalizing $C_1(t)$ to experimental value $C_1(0)$.

3.2. Samples

Samples were a kind gift from AKZO Corporation. We report results on sample $A1$, which is a suspension of TiO_2 particles at initial volume fraction $\Phi_0 = 0.702\%$ in $\simeq 85\%$ H_2O, $\simeq 10\%$ resin and $\simeq 4\%$ organic solvent. Dilutions were made using distilled water. The sedimentation time (of order of 24 hours) of this suspension was much larger than the duration (of order of 30 mn) of a light scattering experiment. $A1$ is shacked and sonicated before the experiment in order to obtain a homogeneous suspension and to eliminate eventually the few large aggregates which tend to form. We have determined the viscosity versus Φ, average particle size, γ, and l^* as follows:

3.2.1. Viscosity versus solid fraction $\eta(\Phi)$

We used a velocity gradient viscosimeter operated at velocity gradients between 6 and 130 s^{-1}, and temperature $T = 298$ K. For all Φ, the viscosity $\eta(\Phi)$ did not depend on the velocity gradient, indicating that the suspension is a Newtonian fluid. From the measurements, we have obtained the extrapolated function[4]: $\eta(x) = \eta_0(1 + 0.63x + 0.425x^2)$ for $10^{-5} \leq x = \Phi/\Phi_0 \leq 1$ and $\eta_0 = 0.906$ cP. Furthermore, the density measured between $T = 293$ and 300 K was independent of Φ, and its value ($\rho = 0.968 \pm 0.014\,g/cm^3$) equal to the density of water. Thus, we know both the dynamic $\eta(x)$ and kinematic $\nu(x)$ viscosity of the suspension.

3.2.2. Average size of TiO_2 particles

We have used the standard QELS technique [9] to determine the particle size. This technique consists of a measurement of the single scattering correlation time τ_0. The particle size is then calculated from the Stokes-Einstein relation. The experiment, made at $\Phi \simeq 7.10^{-5}\%$ and $T = 293.54$ K, revealed a monoexponential decay of $C_1(t)$ indicating that the suspension $A1$ was monodisperse, and the TiO_2 particles have the average diameter $= 0.284\,\mu m$, corresponding to Mie particles [14].

3.2.3. Coefficient γ

γ $(= 1 + \Delta)$ is the distance (in units of transport mean free path) after which the non diffusive light impinging from the outside of the sample is converted into diffusive light inside the sample. The value of Δ depends sensitively on the

[4] Note that the function $\eta(x)$ is different from the Einstein relation [16]: $\eta(x) = \eta_0(1 + 2.5\Phi_0 x)$. This difference is attributed to the change of the reference viscosity η_0 during successive dilutions with water.

transport of light near the sample boundary, and therefore depends on particle size, polarization and skin layer effects [17][5]. For isotropic scattering and for vanishing optical index mismatch between the scattering medium and its surroundings (i.e. in absence of skin layer effects) the scalar value $A_0 = 0.7104$ is obtained from the Milne theory. For real situation of nonzero index mismacth A may be different from A_0. For instance, $A = 0.757$ corresponds to ratio 0.89 of the inner and outer refractive index for a water-glass interface [17]. In order to measure γ, we have performed a multiple light scattering experiment for VV polarization near backscattering from a semi-infinite medium in zero shear. Within the framework of scalar wave theory, one can show (see Eq. (7) with $\tau_c \to \infty$) that γ is the slope of $C_1(t)$ versus $\sqrt{3t/2\tau_0}$ in backscattering. With τ_0 as obtained from the single scattering QELS experiments, we found $\gamma = 1.67$ within 4%. This value of γ is very similar to those given in literature [6,15] for polystyrene spheres in the Mie regime [14] (size $\simeq$ 0.2–0.6 μm). The additional internal reflections from the air-glass interface do not significantly affect our results, as experiments using water instead of air as the outer medium gave identical data.

3.2.4. Transport mean free path versus solid fraction, $l^*(\Phi)$

In order to measure the transport mean free path l^*, we have performed multiple light scattering measurements of $C_1(t)$ in a slab of thickness $L =$ 1 mm in the transmission geometry. To fit the experimental data, we used Eq. (10) with $\tau_p \to \infty$. τ_0 and γ being known from above, the only fitting parameter of $C_1(t)$ is l^* . We obtained: $l^*(x) = 15.92/x$ [μm] ; $0.1 \leq x = \Phi/\Phi_0 \leq 1$.

4. Results and discussion

4.1. Laminar and stationary flows

To test the model described in Section 2, we have performed experiments on laminar shear flow in the planar Couette and planar Poiseuille geometry. For all experiments we used the suspension $A1$ as characterized above.

4.1.1. Planar Couette flow

The Couette cell is sketched in Fig. 1. The inner cylinder is rotating with constant angular velocity Ω and outer cylinder is at rest. Because of the small gap $L/R_2 \simeq 6.7\times10^{-2}$, the effect of curvature of the cylinders on the trajectories of fluid particles can be neglected, and the flow can be described by the planar Couette flow with a linear velocity profile given by: $V_\theta = \Gamma(L-x)$, $0 \leq x \leq L$,

[5] A corresponding to τ_0 of Ref. [17].

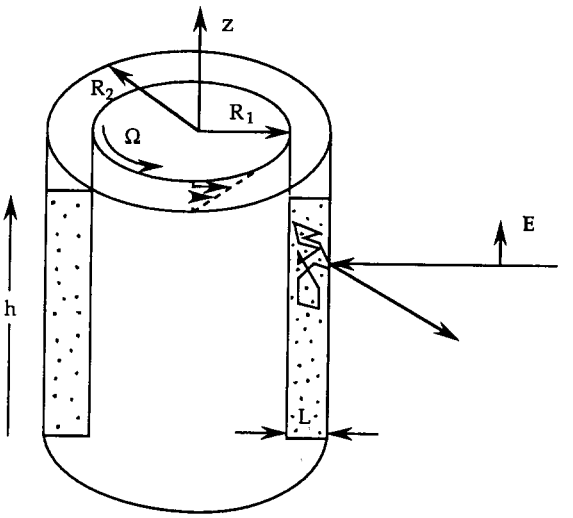

Fig. 1. Sample geometry for Couette flow: The Couette cell consists of two coaxial cylinders. The inner stainless steel cylinder rotates with constant angular velocity Ω, and the outer glass cylinder of thickness 1.5 mm is at rest. $R_1 = 1.26$ cm and $R_2 = 1.35$ cm are the respective outer radius of the inner cylinder and the inner radius of the outer cylinder. The inner cylinder is recovered by black paint to absorb light. $L = R_2 - R_1$ is the gap between cylinders, $h = 9.7$ cm the fluid height in the Couette cell. The horizontal fluid surfaces are free on the upper side and rigid on the lower side. The incident laser beam (of waist $d \simeq 1$ mm), pointing along the radius of the cylinders, impinges on the center of outer cylinder and is vertically polarized. The scattered light is collected on same side of the cell off backscattering.

where $\Gamma = \Omega R_1/L$ is the constant velocity gradient between cylinders. Using a stroboscope system, Ω is measured with accuracy of 0.65%. For the Couette flow, we used the suspension $A1$ at volume fraction 0.117%. The maximum angular velocity used was: $\Omega_{max} = 12.14$ rad/s corresponding to a velocity gradient $\Gamma_{max} = 170\ s^{-1}$ and a Reynolds number of $R = \Omega_{max} R_1 L/\nu = 134$. This Reynolds number is below the critical value $R_c = 156.7$ [18] of the Taylor-Couette instability, so that this experiment probes the laminar flow regime. The dynamic light scattering experiment is carried out in reflection with an extended plane wave source (of waist d such that $d/l^* \simeq 11$). The experimental parameters are given in Table 1.

The goal of this experiment was to measure the velocity gradient in planar Couette flow by the sole analysis of $C_1(t)$. Fig. 2 shows the data for $C_1(t)$ in quiescent state $R = 0$, and a fit to Eq. (7) with $\tau_c \to \infty$. From this we obtained: $\tau_0 = 495\,\mu$s. Also shown are data at increasing values of Ω. Since at time scales (of order of $100\,\mu$s) the Taylor dispersion [12,13] is negligible, τ_0 is not affected by the presence of a velocity gradient, and has thus the same value in curves labelled 1 to 5 in Fig. 2. Fig. 2 illustrates that the decay rate of $C_1(t)$ at long times increases with the velocity gradient, i.e. the correlation time τ_c decreases with Γ. The inset of Fig. 2 shows that

Table 1
Parameters used in the planar Couette flow experiment

Temperature	$T = 296.54$ K
Kinematic viscosity	$\nu = 1.03 \times 10^{-2}$ cm^2/s
Wavelength (in water)	$\lambda = 386.84$ nm
Thickness of slab	$L = 0.9$ mm
Coefficient γ	$\gamma = 1.67$
Scattering mean free path	$l = 45.42$ μm
Transport mean free path	$l^* = 89.07$ μm

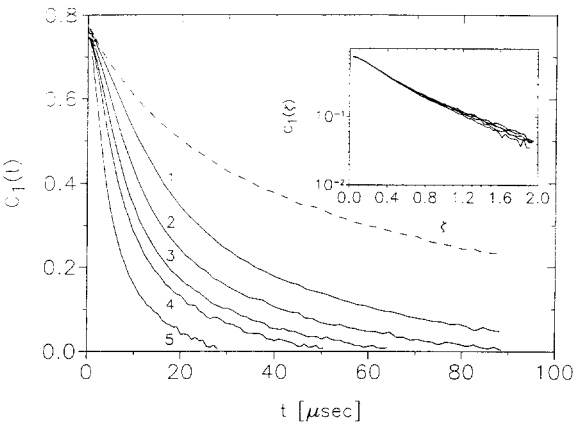

Fig. 2. $C_1(t)$ versus t for reflection geometry. The dashed curve corresponds to Brownian motion alone ($\Gamma = 0$ s^{-1}), and solid curves relate to different values of imposed velocity gradients: (1) $\Gamma = 27$ s^{-1}, (2) $\Gamma = 43.8$ s^{-1}, (3) $\Gamma = 62$ s^{-1}, (4) $\Gamma = 80$ s^{-1}, (5) $\Gamma = 137$ s^{-1}. Inset: $\ln[C_1(\zeta)]$ versus the reduced variable $\zeta = \sqrt{6(t/\tau_c)^2 + (3t/2\tau_0)}$.

curves 1 to 5 superimpose when plotted against the reduced variable $\zeta = \sqrt{6(t/\tau_c)^2 + (3t/2\tau_0)}$, demonstrating that $C_1(t)$ is a function of the sole variable ζ. Fig. 3 shows the data set at $\Gamma = 80$ s^{-1}. The best fit of these data with Eq. (7) (solid curve through the data) gives $\Gamma_{exp} = 86.62$ s^{-1}, whereas the dashed curve corresponds to Eq. (7) plotted with Γ equal to the imposed value. The close agreement between data and Eq. (7) is evident. In Fig. 4 we show Γ_{exp} as obtained by this way for various values of Γ. This plot shows that, within 8.9%, the two measurements of Γ_{exp} and Γ quantitatively agree without any adjustable parameters demonstrating hence the validity of our theory presented in Section 2. The small discrepancy between Γ and Γ_{exp} may be due to skin layer effects [17].

4.1.2. Planar Poiseuille flow

We have also performed experiments in a rectangular flow cell with the sample dimension shown in Fig. 5. Because of the large aspect ratio $h/L = 10$, one can neglect the boundary effects in y direction and consider planar

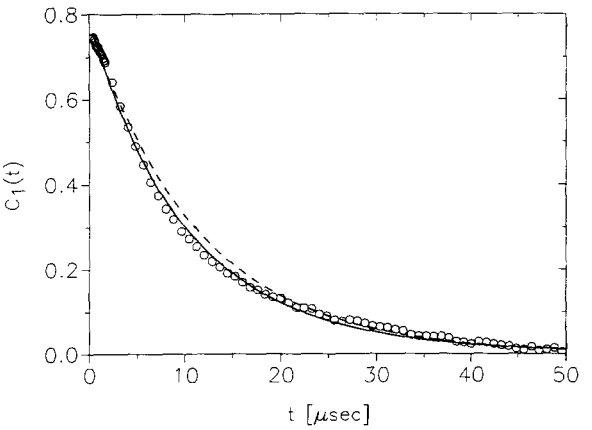

Fig. 3. $C_1(t)$ versus t at imposed $\Gamma = 80\ s^{-1}$ for reflection geometry. The circles are experimental data, and the solid curve corresponds to the best fit of data to Eq. (7) with $\Gamma_{exp} = 86.62\ s^{-1}$. The dashed curve is a plot of Eq. (7) with $\Gamma = 80\ s^{-1}$.

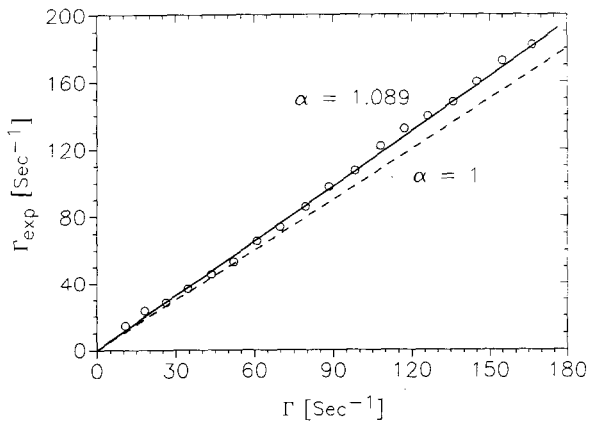

Fig. 4. Γ_{exp} versus Γ. Γ_{exp} is measured using a fit to Eq. (7) and Γ is directly obtained from the measurement of Ω. The experimental data (circles) are well described by a straight line (solid curve) of slope $\alpha = 1.089$.

Poiseuille flow. The velocity profile in z direction is parabolic: $V_z(x) = \frac{\Gamma}{4L}(L^2 - 4x^2)$; $\frac{-L}{2} \leq x \leq \frac{L}{2}$, where $\Gamma = 4V_0/L$. The velocity gradient Γ is related to the flow rate by $Q = hL^2\Gamma/6$. The flow of fluid is obtained by elevation of a large section container (section of container/section of sample cell $\simeq 10^3$) filled with suspension $A1$ above the sample cell. Container and sample cell are connected by a cylindrical tube of the same cross-section of area than the sample cell. Q was obtained by measuring the election volume per time. Suspension $A1$ at volume fraction 0.234% flows through the sample cell at constant flow rate. The maximum flow rate used was: $Q_{max} = 6.67 \times 10^{-2}$ cm^3/s corresponding to $V_0 = 6.25$ cm/s and a Reynolds number $R =$

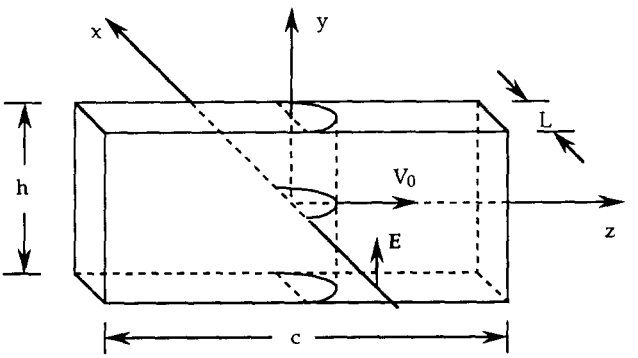

Fig. 5. Sample geometry for planar Poiseuille flow: The rectangular cell is a glass capillary with dimensions: $L = 0.4$ mm , $h = 4$ mm , $c = 90$ mm. V_0, the maximal velocity in the center of the cell, is directly obtained from the measurement of the flow rate Q. The velocity gradient is in x direction. The incident laser beam (of waist $d \simeq 1$ mm), directed along the velocity gradient and vertically polarized, passes through the center of the cell. The scattered light is collected in transmission on the same axis as the incident direction.

Table 2
Parameters used in the planar Poiseuille flow experiment

Temperature	$T = 296.54$ K
Kinematic viscosity	$\nu = 1.15 \times 10^{-2}$ cm^2/s
Wavelength (in water)	$\lambda = 386.84$ nm
Thickness of slab	$L = 0.4$ mm
Coefficient γ	$\gamma = 1.67$
Transport mean free path	$l^* = 44.97\ \mu$m

$V_0 L/2\nu = 10.9$. For Poiseuille flow, this Reynolds number is well below of the turbulent threshold $R_c \simeq 5772$ [19], so that this experiment is in the laminar flow regime. On the other hand, in order to avoid perturbations due to entrance effects [19–21], we have to work at Reynolds number such that the characteristic distance z_1 for entrance effects is smaller than half of the cell length $c/2$. This means: $R \leq 112.5$.

The dynamic light scattering experiment was carried out in the transmission geometry. Since $d/L \simeq 2.5$, the laser beam was considered as an extended plane wave source. Table 2 gives parameters used in this experiment.

Note that the typical number of scattering events is $(L/l^*)^2 \simeq 80$. In order to determine the velocity gradient in inhomogeneous (Poiseuille) flow, we measure the correlation time τ_p defined in Section 2. According to Eq. (8), using the values of L and l^* from Table 2, the effective velocity gradient is $\Gamma_{eff} = 0.4674\Gamma$. Note that this value of Γ_{eff} is about 20% less than a homogeneous averaged velocity gradient. In absence of flow ($\tau_p \to \infty$ in Eq. (10)) we measured the Brownian correlation time: $\tau_0 = 583\,\mu$s. This time remains constant in the presence of velocity gradients because of the negligible correction of the Taylor dispersion [12,13]. A typical result with

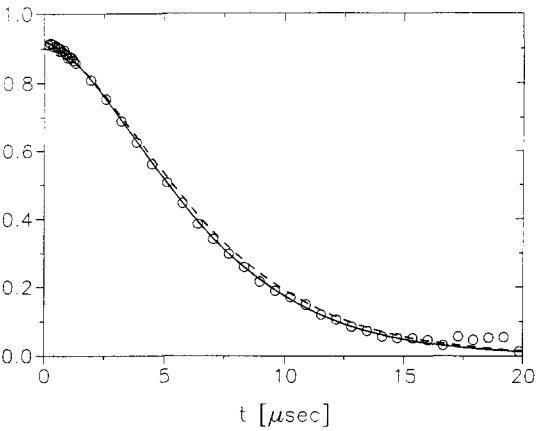

Fig. 6. $C_1(t)$ versus t at imposed $\Gamma = 246.75\ s^{-1}$. The circles are experimental data for transmission geometry. The solid curve corresponds to the best fit of data to Eq. (10) with $\Gamma_{exp} = 257.58\ s^{-1}$. The dashed curve is the plot of Eq. (10) with a velocity gradient equal to the imposed value $\Gamma = 246.75\ s^{-1}$.

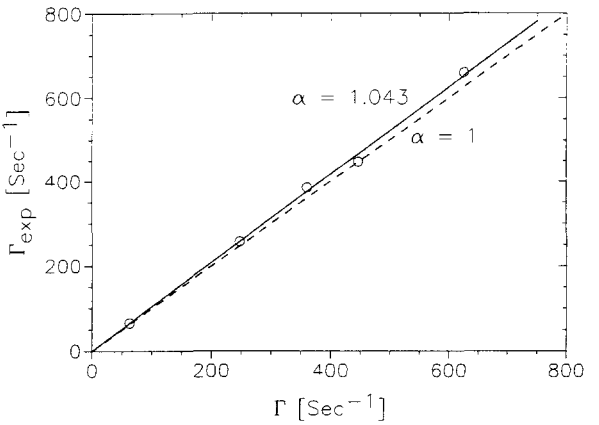

Fig. 7. Γ_{exp} versus Γ. Γ_{exp} is measured using $C_1(t)$ and Γ is directly obtained from the measurement of flow rate Q. The experimental data (circles) are well described by a straight line (solid curve) of slope $\alpha = 1.043$. The expected straight line of slope $\alpha = 1$ (dashed curve) is shown for comparison.

an imposed velocity gradient $\Gamma = 246.75\ s^{-1}$ is shown in Fig. 6 . The best fit to Eq. (10) (solid curve through the data) gives $\Gamma_{exp} = 257.58\ s^{-1}$. The dashed curve corresponds to Eq. (10) plotted with Γ equal to the imposed value. It appears that the data are well described by the theory of Section 2. Furthermore, over the entire range of accessible shear rates, the measured time autocorrelation functions are well fitted by Eq. (10) with τ_p (or Γ) the only fitting parameter. In Fig. 7 we have plotted Γ_{exp} as obtained from these fits versus Γ. The result agrees within 4.3% with the theory [7,8] note that the

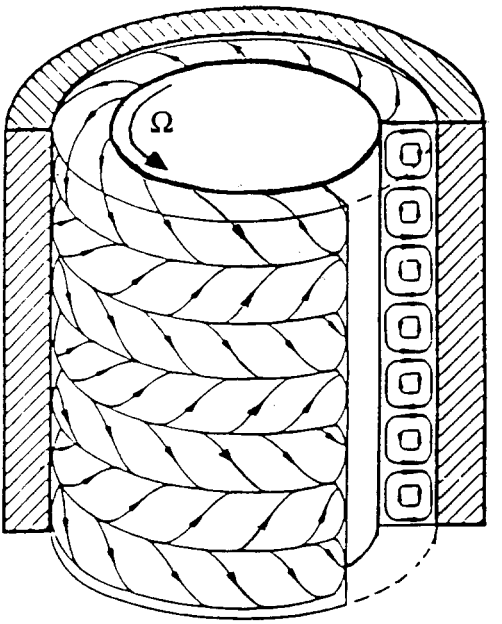

Fig. 8. Schematic diagram of Taylor-Couette flow above R_c.

parameter γ is also known within about 4%. This confirms the functional form of the time autocorrelation function despite of the inhomogeneous velocity gradient. In other words, for Poiseuille flow the time autocorrelation function has the same functional form as the one for a homogeneous system of identical size, provided that Γ is replaced by Γ_{eff}. This also implies that the average velocity gradient for inhomogeneous shear is well described by introducing the local density distribution of diffusion paths.

4.2. Taylor-Couette instability

For small Reynolds numbers, Taylor-Couette flow in an infinitely long system has only an azimuthal velocity component. This is so-called circular Couette flow (CCF) was studied in the previous subsection. We now consider Couette flow at higher Reynolds numbers [22]. At the critical Reynolds $R = R_c$ [22], a centrifugal instability gives rise to time-independent Taylor vortex flow (TVF). TVF (Fig. 8) consists of a sequence of pairs of counter-rotating toroidal vortices (the vortex width is roughly equal to the gap L between cylinders) stacked along the cylinders. The velocity varies periodically (with a period $2L$) along the system axis, and is constant in the azimuthal direction. At $R = 1.2R_c$ appears a first time-dependent regime, wavy vortex flow (WVF), in which an azimuthal travelling wave is superimposed on the TVF. The velocity power spectrum contains a single frequency, ω_1, and the flow is strictly periodic.

Table 3
Couette cell system with inner cylinder rotating and outer cylinder at rest

Inner cylinder radius	$R_1 = 1.25$ cm
Outer cylinder radius[a]	$R_2 = 1.37$ cm; $R_2 = 1.59$ cm
Ratio of radii[a]	$R_1/R_2 = 0.912$; $R_1/R_2 = 0.786$
Fluid height	$h = 9.7$ cm
Height/gap[a]	$h/L = 80.83$; $h/L = 28.53$
Critical Reynolds number[a]	$R_c = 135.7$; $R_c = 84.2$

[a] The first and second values correspond to a small and large gaps, respectively.

Table 4
Values of parameters used for Taylor-Couette flow experiment

Temperature	$T = 296$ K
Kinematic viscosity	$\nu = 1.11 \times 10^{-2}$ cm^2/s
Wavelenght (in water)	$\lambda = 386.84$ nm
Waist of beam	$d \simeq 1$ mm
Thickness of slab[a]	$L = 1.2$ mm; $L = 3.4$ mm
Coefficient γ	$\gamma = 1.67$
Transport mean free path	$l^* = 44.97$ μm
Brownian correlation time	$\tau_0 = 734.5$ μs

[a] Same meaning as in Table 3.

Above $R \simeq 10\,R_c$ further instabilities appear involving additional frequencies leading ultimately to weakly turbulent flow [22]. This study does not concern $R > 10\,R_c$. Our aim is to study the Taylor-Couette instability using the velocity gradient measurement. Since the fundamental frequencies (e.g. ω_1) and their harmonics of weak amplitude are small compared to τ^{-1} and τ_0^{-1} (we always have[6] $\omega_i\tau \leq 10^{-4}$–$10^{-3}$) the flow is quasi-stationary at time scales τ and τ_0. Our technique allows in principle to determine the critical Reynolds number R_c, the wavenumber q ($\simeq \pi/L$) of the periodic state, and the R-dependence of the velocity gradient within the instability regime. For a laser beam diameter, d, smaller than the size of the Taylor roll ($d < L$), the spatial periodicity of the flow can be measured, whereas for a large beam ($d > L$) the dependence of $\langle \Gamma^2 \rangle$ on R can be determined. The experiment was performed using the same set-up as before (see Fig. 1) in reflection geometry using as extended plane wave source a about 1 mm diameter laser beam. The parameters of the Couette cell are given in Table 3.

The fluid was suspension $A1$ at volume fraction 0.1755%. The sample parameters used in the experiment are listed in Table 4.

[6] Since ω_1 is of order of Ω (harmonics are of smaller amplitude [22]) one can write: $\omega_1\tau \simeq \Omega\tau \simeq L\Omega/kl^*R_1\Omega_{eff}$. The highest value of Ω/Ω_{eff}, corresponding to laminar regime, is: $\Omega/\Omega_{eff} = 1$. We have in this experiment: $kl^* \simeq 10^3$ (weak scattering limit), $L/R_1 \simeq 0.1 - 0.3$ (small and large gaps), then we obtain: $\omega_1\tau \leq 10^{-4}$–$10^{-3}$.

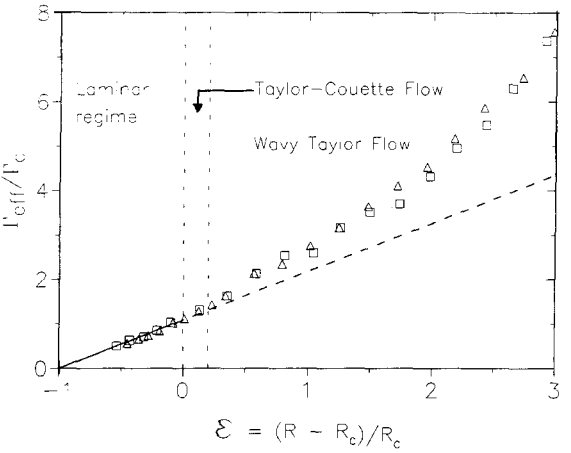

Fig. 9. Reduced effective velocity gradient Γ_{eff}/Γ_c versus the reduced Reynolds number $\epsilon = R/R_c - 1$ using a large beam ($d/L \simeq 1$). The triangles and squares are the experimental data measured at different z values of the incident beam. The straight line (of slope 1.089) corresponds to the linear behaviour in the laminar regime (see Fig. 4).

The measurement of velocity gradient is obtained by the same procedure described above (Section 4.1), i.e. we determine the correlation time $\tau = \sqrt{30}/kl^*\Gamma_{eff}$ of $C_1(t)$ (with τ_c replaced by τ), by fitting the experimental data with Eq. (7). Since the parameters of Table 4 entering $C_1(t)$ are the same for all experiments, τ is the only fitting parameter.

4.2.1. Small gap $L \leq d$: homogeneous effective velocity gradient

Fig. 9 shows Γ_{eff}/Γ_c versus ϵ, where $\Gamma_c = \Omega_c R_1/L = 101.5\ s^{-1}$ is the velocity gradient corresponding to the critical Reynolds number. It clearly appears that, above $\epsilon = 0$, the experimental data deviate from the solid curve corresponding to the linear behaviour of the laminar regime. The second instability, towards wavy vortex flow, is not visible in this data. This may be due to the smallness of additional shear and to the fact that $C_1(t)$ is averaged over many periods of the wavy flow [22]. According to the Appendix B, the excess shear Γ_{TV} due to the Taylor vortices can be written as:

$$\frac{\Gamma_{TV}}{\Gamma_c} = \sqrt{\left(\frac{\Gamma_{eff}}{\Gamma}\right)^2 - 1} = \sqrt{\alpha\epsilon'} \tag{12}$$

Fig. 10 shows Γ_{TV}/Γ_c versus the reduced Taylor number $\epsilon' = (T - T_c)/T_c$. The experimental data are well described by Eq. (12) (with $\alpha = 0.13$) which is consistent with the prediction by Landau [19,24]. A similar conclusion for Couette flow has been arrived at by Donnelly [25]. It may appear surprising that, although Eq. (12), and Eqs. (B.9), (B.11), (B.13) of Appendix B apply only for $\epsilon' \ll 1$, our data suggest that these expressions may be valid even

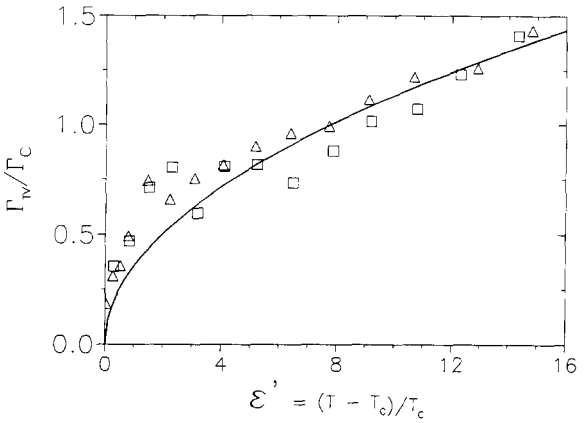

Fig. 10. Reduced velocity gradient of Taylor vortices Γ_{TV}/Γ_c versus the reduced Taylor number $\epsilon' = T/T_c - 1$. The legend is the same than in Fig. 9. The solid curve is the best fit of the experimental data to Eq. (12), with $\alpha = 0.13$.

far above the onset of the Taylor vortex flow. Torque measurement by Davey [24] also suggested such behavior well beyond the range of applicability of the perturbation theory. From this point of view, the theory presented in Appendix B seems sufficient to describe our data. This provides a new way to determine the transition from laminar to Taylor vortex flow. However, a plot of $\ln(\Gamma_{eff})$ versus $\ln(R)$ reveals (see Fig. 14) that the same data are also consistent with a power law $\Gamma_{eff}/\Gamma_c = (R/R_c)^{\delta}$, as suggested by Måløy and Golburg [26]. For the data obtained with a large beam (Fig. 14(a)), we find $\delta = 1.26$ which is very close to the findings $\delta = 1.25$ [26] obtained from the average velocity gradients.

We have also measured Γ_{eff} as a function of height z. Fig. 9 shows two sets of experimental data (circles and squares) obtained at different points of height separated by 0.55 mm $\simeq L/2$. There is no difference between these curves, indicating that the effective velocity gradients as measured with a large beam are homogeneous.

4.2.2. Large gap $L > d$: quasi-local effective velocity gradient

We have also performed velocity gradient measurements using a much smaller beam. Fig. 11 shows Γ_{eff}/Γ_c versus ϵ, measured at two different heights separated by about $L/2$. In this experiment the critical velocity gradient is $\Gamma_c = 8.26\ \mathrm{s}^{-1}$. Like before Γ_{exp} deviates at large R from the linear behaviour at small R. In addition, as shown in the inset of Fig. 11, the two curves clearly split at the point $\epsilon \simeq 0$, indicating that there is a transition from the uniform state (circular Couette flow) to a nonuniform state (Taylor vortex flow). The analysis of the ϵ-dependence of each curve according to the procedure used in the case of small gap leads to the same conclusions as above.

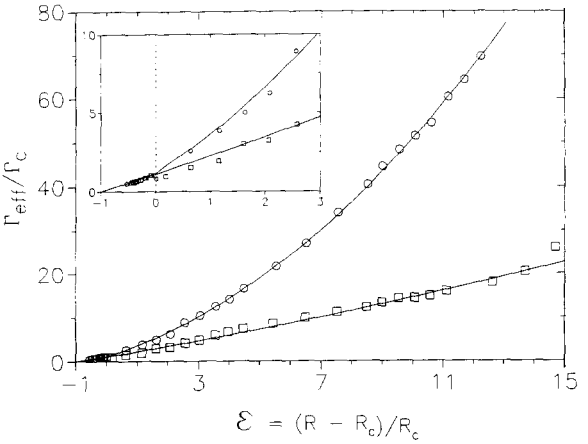

Fig. 11. Γ_{eff}/Γ_c versus ϵ measured at different z values of the incident beam separated by about $L/2$, using a small beam ($d/L \simeq 0.3$). The solid curves are best fits of experimental data to Eq. (B.13) of Appendix B with: $\beta_1 = 0.93$, $\beta_2 = 0.058$ for the upper curve and $\beta_1 \simeq 0$, $\beta_2 = 0.0043$ for the lower one.

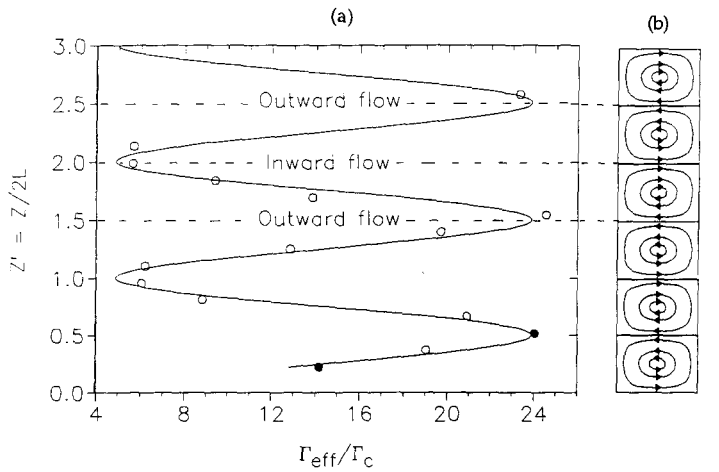

Fig. 12. (a) Γ_{eff}/Γ_c versus $z' = z/2L$ at fixed $R \simeq 6.5\,R_c$, $2L$ being the period of Taylor vortices. Solid curve through the data is the best fit of experimental data using Eq. (B.11) of Appendix B with: $A_1 = 9.5\,\Gamma_c$, $B_1 = 14.39\,\Gamma_c$ and $q = (\pi/3.337)$ mm^{-1}. The origin of z' is arbitrarly chosen. (b) Sketch of stream lines of the Taylor-Couette flow with the inner cylinder rotating and the outer cylinder at rest.

In contrast, the z-dependence at given ϵ is fundamentally different, as shown in Fig. 12(a) where we plot Γ_{eff}/Γ_c versus $z' = z/2L$ at fixed $R \simeq 6.5\,R_c$. It clearly appears that Γ_{eff} is a periodic function with period $2L$ corresponding to the diameter of two Taylor rolls. The best fit (solid curve of Fig. 12(a)) of the data to Eq. (B.11) of Appendix B provides a wavenumber $q = \pi/L$ within 0.9%, and $A_1 = 9.5\,\Gamma_c$, $B_1 = 14.39\,\Gamma_c$. The amplitude of this spatial modu-

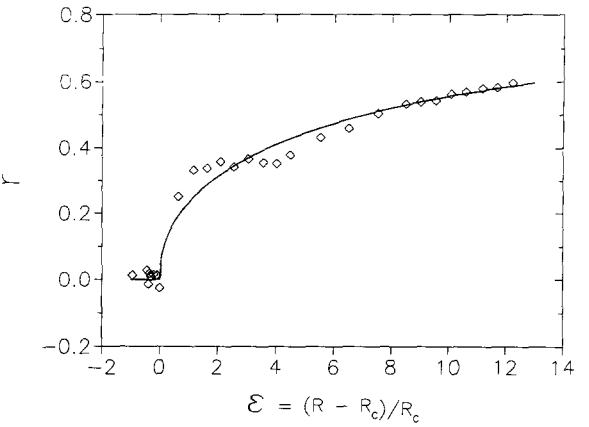

Fig. 13. Shown is the relative amplitude of the periodic part of Γ_{eff}, given as the ratio r (see the text), versus ϵ. The solid curve through the data is obtained from best fits of the data used in Fig. 11.

lation of Γ_{eff} appears very large, indicating that velocity gradients strongly differ between regions of outward directed flow and inward directed flow. In fact, direct visualisation of the flow field by video- microscopic observation of a dilute suspension of plate-like microparticles (kalliroscope) rotated at the same frequency inside our couette cell clearly reveals that the overall local velocity, and hence the relevant gradient, is highest/lowest in regions of strong outward/inward flow respectively, i.e., near separatrices between rolls. Unfortunately this video method does not provide quantitative measurement of the velocity gradient. Our results (Fig. 12) are in agreement with the velocity gradient measurements [26] obtained from single light scattering, with respect to both amplitude and period of the spatial modulation.

The transition to TVF is also detected by measuring the ratio of Γ_{eff} at two points separated in height by about $L/2$ as a function of Reynolds number. In Fig. 13 we plot the relative amplitude of the periodic part of Γ_{eff}, given as $r = (r_1 - 1)/(r_1 + 1)$ with $r_1 = \Gamma_{eff}(z_1')/\Gamma_{eff}(z_2')$, versus ϵ, for $z_1' = 0.52$ and $z_2' = 0.23$ corresponding to the two black points indicated in Fig. 12(a). Like in Fig. 10, we find that the ratio r becomes different from zero near $\epsilon = 0$. Its sudden increase for $\epsilon > 0$ is the signature of the transition to TVF according to Landau's law [19,24] (solid curve). Alternatively, our data using a small beam can be fitted very well to a power law, as above, but the δ value now depends on the vertical position of the beam (see Figs. 14(b) and (c)).

Thus, by the simple velocity gradient measurement, it is possible to determine not only the threshold of the Taylor-Couette instability but also to study the additional velocity components associated with the Taylor vortices on a quasi-local scale. In addition, it appears possible to determine the wavenumber of the Taylor rolls from Γ_{eff}, despite of the fact that the rolls are not visible by

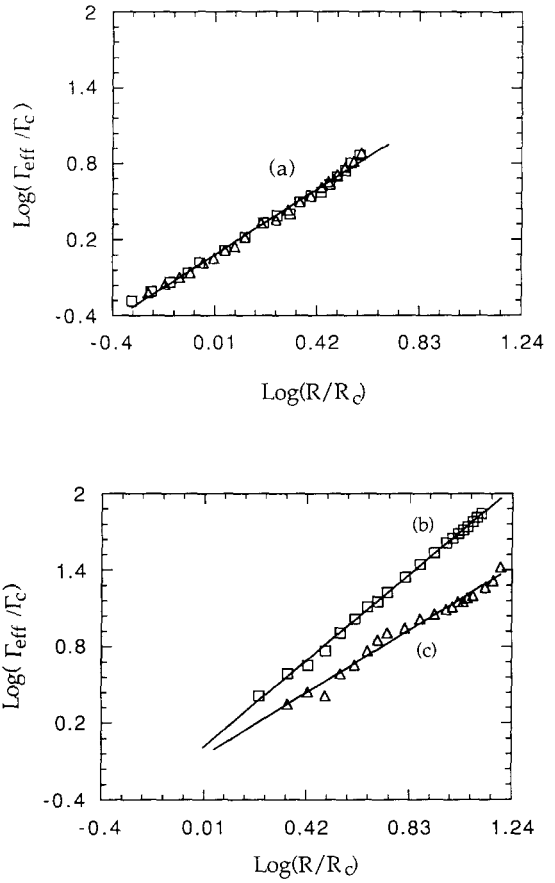

Fig. 14. Log-Log plot shows the dependence of the effective velocity gradient on the Reynolds number.
Large beam (a): Open triangles and squares correspond to experimental data of Fig. 9 . The solid line, with the slope $\delta = 1.26$, is the best linear fit to the data.
Small beam: Open circles and squares for (b) and (c), respectively, correspond to experimental data of Fig. 11. The best linear fits (solid lines) have slopes $\delta = 1.64$ and $\delta = 1.19$ for (b) and (c), respectively.

eye, as the colloidal fluid remains essentially homogeneous.

5. Conclusion

We have shown experimentally, that dynamic *multiple* light scattering experiments provide an accurate and non-invasive method to measure velocity gradients. Analysis of the time autocorrelation function $C_1(t)$ using a simple model provides the shear correlation time $\tau \propto 1/kl^*\Gamma_{eff}$. This model could be refined to incorporate skin layer effects which, however, turn out to be neg-

ligible in our experiments. This technique has been extended into the regime of hydrodynamic instabilities. Indeed, the critical Reynolds number R_c and wavenumber q of the Taylor-Couette instability was measured by this way, despite of the fact that the Taylor vortices are not visible by eye, because of the homogeneous turbidity of the fluid. The dependence of the measured shear gradient Γ_{eff} on the Reynolds number is in agreement with Landau's model. It appears interesting to extend this technique to turbulent flow, where shear gradients could be probed at the (experimentally adjustable) length scale of the transport mean free path l^*.

Acknowledgement

We are pleased to thank R. Maynard for fruitful discussions, and B. Tinland, W. Leutz, F. Erbacher and R. Lenke for their help during the experiments.

Appendix A

The dephasing of light originating from the change of the diffusion path length caused by scatterers which follow the flow is given by [3,8,11]:

$$\Delta\phi_n(t) = k\,t \sum_{\nu=1}^{n} \boldsymbol{e}_\nu \cdot [\mathbf{V}(\mathbf{r}_\nu) - \mathbf{V}(\mathbf{r}_{\nu+1})] \tag{A.1}$$

where $\boldsymbol{e}_\nu$ is the emergent unit vector from the ν^{th} scattering joining $\mathbf{r}_\nu$ and $\mathbf{r}_{\nu+1}$ ($\langle|\mathbf{r}_\nu - \mathbf{r}_{\nu+1}|\rangle = l$ by definition), and $\mathbf{V}(\mathbf{r}_\nu)$ is the velocity of the ν^{th} scatterer. According to assumptions *i)* and *ii)* of Section 2, it has been shown [8] that Eq. (A.1) can be rewritten as:

$$\Delta\phi_n(t) = -klt \sum_{\nu=1}^{n} \sum_{i,j} A_{ij}(\nu)\,\sigma_{ij}(\mathbf{r}_\nu); \qquad i,j = x,y,z \tag{A.2}$$

where $A_{ij}(\nu) = e_{\nu i} e_{\nu j}$ is the random scattering symmetric tensor which depends only upon the ν^{th} scattering angles, and σ_{ij} is the strain tensor. For incompressible fluids (div $\mathbf{V} = 0$), the computation of $C_1(t)$ requires to calculate fluctuations $\langle\Delta\phi_n^2(t)\rangle$ of the dephasing of light. We then consider the quantity:

$$\langle\Delta\phi_n^2(t)\rangle = (klt)^2 \sum_{\nu,\nu'=1}^{n} (1 + \delta_{\nu\nu'}) \times \left\{ \sum_{i,j} \sum_{k,l} \overline{A_{ij}(\nu)\,A_{kl}(\nu')} \langle\sigma_{ij}(\mathbf{r}_\nu)\sigma_{kl}(\mathbf{r}_{\nu'})\rangle \right\} \tag{A.3}$$

where $\overline{\cdots}$ denotes the average upon scattering angles whereas $\langle \cdots \rangle$ indicates the average obtained from the weighting over the cloud of diffusion paths [7,8]. When the scattering is anisotropic (Mie scatterers), correlations between scattering vectors can be written as:

$$\overline{\boldsymbol{e}_\nu . \boldsymbol{e}_{\nu'}} = \overline{e_\nu^2} \left(\overline{\cos\theta}\right)^{|\nu-\nu'|} \tag{A.4}$$

where θ is the angle between $\boldsymbol{e}_\nu$ and $\boldsymbol{e}_{\nu'}$. $\boldsymbol{e}_\nu$ are averaged over the unit sphere and:

$$\overline{\cos\theta} = \frac{\int_0^\pi F(\theta) \cos\theta \sin\theta \, d\theta}{\int_0^\pi F(\theta) \sin\theta \, d\theta} \tag{A.5}$$

$F(\theta)$ being the form factor[15]. Thus, the tensor $\overline{A_{ij}(\nu) A_{kl}(\nu')}$ can be written as:

$$\overline{A_{ij}(\nu) A_{kl}(\nu')} = \frac{\delta_{ij}\delta_{kl}}{9} + \frac{\left(\overline{\cos\theta}\right)^{|\nu-\nu'|}}{15} \times \left\{ \left(\overline{\cos\theta}\right)^{|\nu-\nu'|} \delta_{ij}\delta_{kl} + \delta_{ik}\delta_{jl} + \delta_{il}\delta_{jk} \right\} \tag{A.6}$$

Replacing (A.6) into (A.3), we have:

$$\langle \Delta\phi_n^2(t) \rangle = \frac{4(klt)^2}{15} \sum_{\nu=1}^{n} \sum_{i,j} \langle \sigma_{ij}^2(\mathbf{r}_\nu) \rangle \times \left(1 + \sum_{\nu'=\nu+1}^{n} \left(\overline{\cos\theta}\right)^{|\nu-\nu'|} \right) \tag{A.7}$$

For $n \gg 1$, Eq. (A.7) can be rewritten as:

$$\begin{aligned} \langle \Delta\phi_n^2(t) \rangle &= \frac{4(klt)^2}{15} \sum_{\nu=1}^{n} \sum_{i,j} \langle \sigma_{ij}^2(\mathbf{r}_\nu) \rangle \left(1 + \sum_{\nu'=1}^{\infty} \left(\overline{\cos\theta}\right)^{\nu'} \right) \\ &= \frac{4(kt)^2}{15} \frac{l^2}{1-\overline{\cos\theta}} \sum_{\nu=1}^{n} \left(\sum_{i,j} \langle \sigma_{ij}^2(\mathbf{r}_\nu) \rangle \right) \end{aligned} \tag{A.8}$$

Rescaling $\nu l = \nu^* l^*$ and $nl = n^* l^*$, where ν^* and n^* are, respectively, the index and the total number of independent scattering events, and $l^* = l/(1-\overline{\cos\theta})$ being the transport mean free path, (A.8) becomes:

$$\langle \Delta\phi_n^2(t) \rangle = \frac{4(kl^*t)^2}{15} \sum_{\nu^*=1}^{n^*} \left(\sum_{i,j} \langle \sigma_{ij}^2(\mathbf{r}_{\nu^*}) \rangle \right) \tag{A.9}$$

Eq. (A.9) obtained above is exactly the same than the expression obtained for pointlike scatterers provided that l is everywhere replaced by l^*. Since $\sigma_{ij}(\mathbf{r}_{\nu^*})$

is now evaluated at the scale l^*, the expression of $\langle \Delta\phi_n^2(t) \rangle$ is therefore only valid for the velocity field which varies slowly at the scale l^*. In this case, the dephasing of light for Mie scatterers can be approximated by:

$$\Delta\phi_n(t) \simeq k\,t \sum_{\nu^*=1}^{n^*} \boldsymbol{e}_{\nu^*} \cdot [\mathbf{V}(\mathbf{r}_{\nu^*}) - \mathbf{V}(\mathbf{r}_{\nu^*+1})] \tag{A.10}$$

with $\langle |\mathbf{r}_{\nu^*} - \mathbf{r}_{\nu^*+1}| \rangle = l^*$ by definition.

Appendix B

In this appendix we derive the expression of the effective velocity gradient Γ_{eff} for flow above the Taylor-Couette instability. Γ_{eff} is defined by the relation:

$$\Gamma_{eff}^2 = 2 \sum_{ij} \langle \sigma_{ij}^2 \rangle \tag{B.1}$$

where $i, j = x, y, z$, σ_{ij} is the strain tensor of the velocity field and the average $\langle \cdots \rangle$, representing the integral of Eq. (3) of the main text, is obtained from the density distribution of diffusion paths in reflection $\rho_n(\mathbf{r})$ [7,8].

The control parameter for the Taylor-Couette instability with the outer cylinder at rest is the Taylor number T, which for $L \ll (R_2 + R_1)/2$ [18] is related to the Reynolds number R by:

$$T = \frac{4L^2}{R_2^2 - R_1^2} R^2 \cong \frac{2L}{R_1} R^2 \tag{B.2}$$

The critical Taylor number is $T_c = 3390$ [18]. In the vicinity of T_c, the velocity field can be described as:

$$\mathbf{V}_{TVF}(\mathbf{r}, t) = \mathbf{V}_{CCF}(\mathbf{r}) + \mathbf{V}_1(\mathbf{r}, t) \tag{B.3}$$

where $\mathbf{V}_{CCF}(\mathbf{r})$ and $\mathbf{V}_{TVF}(\mathbf{r}, t)$ are velocity fields for Circular Couette Flow and Taylor Vortex Flow, and $\mathbf{V}_1(\mathbf{r}, t)$ is the perturbative velocity field. Because of the periodicity of TVF along the axial direction, the linear theory gives [18,24] $(0 \leq x \leq L)$:

$$\mathbf{V}_1(\mathbf{r}, t) = \begin{cases} A(t)\, u(x) \cos(qz) \\ A(t)\, v(x) \cos(qz) \\ A(t)\, w(x) \sin(qz) \end{cases} \tag{B.4}$$

where u, v and w, the eigenfunctions of the velocity field, are suitably normalized. $q = \pi/L$ (with L being also the size of a Taylor roll) is the critical

wavenumber and $A(t)$ is the complex amplitude of Taylor vortices in flow pattern. The experimental evidence[7] suggests that for $T \geq T_c$, the flow is in the steady state, so that the amplitude of vortices considered here is their equilibrium amplitude A_e given by Landau's law [19,24]:

$$A_e = const. \times \sqrt{\epsilon'}; \qquad \epsilon' = \frac{T - T_c}{T_c} \tag{B.5}$$

Thus, the quasi-stationary velocity field of TVF can be written as:

$$\mathbf{V}(x,y,z) = \begin{cases} A_e\, u(x)\, \cos(qz) \\ \Gamma x + A_e\, v(x)\, \cos(qz) \\ A_e\, w(x)\, \sin(qz) \end{cases} \tag{B.6}$$

where Γ is the velocity gradient of non perturbed circular Couette flow. If we assume that v scales like ΓL the scale for u is $\nu\Gamma L/\Gamma L^2$ according to the (linearized) Navier-Stokes equations such v/u scales like the Reynolds number $\Gamma L^2/\nu = R$. The condition of the incompressible fluid leads to the same scale for u and w. According to Eq. (B.1) and Eq. (B.6), we have:

$$\Gamma_{eff}^2 = \Gamma^2 + a_1 A_e \Gamma \langle \cos(qz) \rangle + a_2 A_e^2 \langle \cos^2(qz) \rangle + a_3 A_e^2 \langle \sin^2(qz) \rangle \tag{B.7}$$

where the constant a_i are the mean values of the square of strain tensor averaged over x variable only. The comparison between the size L of the Taylor rolls and the waist d of the incident laser beam allows us to distinguish small and large gaps:

i) Small gap, large beam: $L \leq d$

In this case the light paths are smeared out over more than one Taylor vortex so that the average of the sine and cosine of Eq. (B.7) are numbers. Γ_{eff} have lost information about the periodic pattern of TVF. Consequently, Γ_{eff} does not depend on the variable z, and is the same everywhere along the axis direction. Since light paths visit more than one of Taylor vortex, one have on average: $\langle \cos(qz) \rangle \simeq 0$. With use of Eq. (B.5) we may write:

$$a_2 A_e^2 \langle \cos^2(qz) \rangle + a_3 A_e^2 \langle \sin^2(qz) \rangle = \Gamma^2 \alpha \epsilon' \tag{B.8}$$

α being a constant, and from Eqs. (B.7)–(B.8), we then obtain:

$$\Gamma_{eff}(\epsilon') = \Gamma \sqrt{1 + \alpha \epsilon'}; \qquad \epsilon' \geq 0 \tag{B.9}$$

ii) Large gap, small beam: $L > d$

[7] see footnote 6.

Now, the main light paths are confined within a small region of space compared to L, so that velocity gradients are roughly constant at the scale d. One can then reasonably replace in Eq. (B.7), $\langle \sin(\cdots)\rangle$ and $\langle \cos(\cdots)\rangle$ by $\sin(\cdots)$ and $\cos(\cdots)$, respectively. We have:

$$\Gamma_{eff}^2(z,\epsilon') = \Gamma^2 + a_1 A_e \Gamma \cos(qz) + a_2 A_e^2 \cos^2(qz) + a_3 A_e^2 \sin^2(qz) \tag{B.10}$$

Furthermore, we know that: $a_1 = \langle \partial_x v\rangle$, and $a_2, a_3 \simeq \langle (\partial_x u)^2 + (\partial_x v)^2 + (\partial_x w)^2\rangle$; we have then: $|a_1|\Gamma/a_2 \sim |V_{CCF}|/|V_1| > 1$, which implies that the leading oscillating term of (B.10) is the factor of $\cos(qz)$. Hence Γ_{eff} is a periodic function with period $2\pi/q = 2L$ which has the form:

$$\Gamma_{eff}(z,\epsilon') = A_1(\epsilon')\cos[q(z - z_0)] + B_1(\epsilon') \tag{B.11}$$

where functions A_1 and B_1 are related to a_i. The ϵ'-dependence of Γ_{eff} is obtained as above:

$$\left.\begin{aligned} a_1 A_e \cos(qz) &= \Gamma \beta_1(z)\sqrt{\epsilon'} \\ a_2 A_e^2 \cos^2(qz) + a_3 A_e^2 \sin^2(qz) &= \Gamma^2 \beta_2(z)\epsilon' \end{aligned}\right\} \tag{B.12}$$

$\beta_1(z)$ and $\beta_2(z)$ ($|\beta_1| > \beta_2$) are periodic functions with periods $2L$ and L, respectively. The effective velocity gradient becomes now:

$$\Gamma_{eff}(z,\epsilon') = \Gamma\sqrt{1 + \beta_1(z)\sqrt{\epsilon'} + \beta_2(z)\epsilon'}; \qquad \epsilon' \geq 0 \tag{B.13}$$

References

[1] G.G. Fuller, J.M. Rallinson, R.L. Schmidt and L.G. Leal, J. Fluid. Mech. 100 (1980) 555.
[2] P. Tong, W.I. Golburg and C.K. Chan, Phys. Rev. A 37 (1988) 2125.
[3] X-L. Wu, D.J. Pine, P.M. Chaikin, J.S. Huang and D.A. Weitz, J. Opt. Soc. Am. B 7 (1990) 15.
[4] G. Maret, P.E. Wolf, Z. Phys. B 65 (1987) 409.
[5] D.J. Pine, D.A. Weitz, P.M. Chaikin and E. Herbolzheimer, Phys. Rev. Lett. 60 (1988) 1134.
[6] D.J. Pine, D.A. Weitz, P.E Wolf, G. Maret, E. Herbolzheimer and P.M. Chaikin, Scattering and Localization of Classical Waves in Random Media, Ed. Ping Sheng (World Scientific, 1990) p.312.
[7] D. Bicout, Ph. D. Thesis J. Fourier University, Grenoble, France (1992).
[8] D. Bicout and R. Maynard, Physica A 199 (1993) 387.
[9] B.J. Berne and R. Pecora, Dynamic Light Scattering: With Applications to Chemistry, Biology, and Physics (Wiley, New York, 1976).
[10] E. Akkermans, P.E. Wolf, R. Maynard and G. Maret, J. Phys. France 49 (1988) 77.
[11] D. Bicout, E. Akkermans and R. Maynard, J. Phys. I France 1 (1991) 471.
[12] G.I. Taylor, Proc. Roy. Soc. A 219 (1953) 186; 223 (1954) 446; 225 473.
[13] C. Van Den Broek, Physica A 116 (1982) 448.
[14] H.C. Van de Hulst, Light Scattering by Small Particles (Dover, New York, 1981).
[15] P.E. Wolf, G. Maret, E. Akkermans and R. Maynard, J. Phys. France 49 (1988) 63.

[16] A. Einstein, Ann. Physik 17 (1905) 549; 34 (1911) 591.
[17] Th. M. Nieuwenhuizen and J.M. Luck, Phys. Rev. E 48 (1993) 569.
[18] S. Chandrasekhar, Hydrodynamic and Hydromagnetic Stability (Dover, New York, 1981).
[19] L. Landau et E. Lifchitz, Mécanique des fluides, Chap. III, 2nd édition (Ed. Librairie du Globe, Edition MIR, 1989).
[20] E. Guyon, J.-P. Hulin et L. Petit, Hydrodynamique Physique (InterEditions/Editions du CNRS, 1991).
[21] H. Schlichting, Boundary-Layer Theory, 7^{th} Edition (McGraw-Hill, 1979).
[22] P.R. Fenstermacher, Harry L. Swinney and J.P. Gollub, J. Fluid Mech. 94 (1979) 103; M. Gorman and H.L. Swinney, J. Fluid. Mech. 117 (1982) 123.
[23] D. Coles, J. Fluid. Mech. 21 (1965) 385.
[24] A. Davey, J. Fluid. Mech. 14 (1962) 336.
[25] R.J. Donnelly, Phys. Rev. Lett. 10 (1963) 282.
[26] K.J. Måløy and W. Goldburg, Phys. Rev. E 48 (1993) 322.